Title
Enhanced dynamic nuclear polarization via swept microwave frequency combs

Journal
Proceedings of the National Academy of Sciences of the United States of America, 115(42)

ISSN
0027-8424

Authors
Ajoy, A
Nazaryan, R
Liu, K
et al.

Publication Date
2018-10-16

DOI
10.1073/pnas.1807125115

Peer reviewed

Enhanced dynamic nuclear polarization via swept microwave frequency combs

A. Ajoy[a,b,1], R. Nazaryan[a,b], K. Liu[a,b], X. Lv[a,b], B. Safvati[a,b], G. Wang[a,b], E. Druga[a,b], J. A. Reimer[b,c], D. Suter[d], C. Ramanathan[e], C. A. Meriles[f], and A. Pines[a,b,1]

[a]Department of Chemistry, University of California, Berkeley, CA 94720; [b]Materials Science Division, Lawrence Berkeley National Laboratory, Berkeley, CA 94720; [c]Department of Chemical and Biomolecular Engineering, University of California, Berkeley, CA 94720; [d]Fakultät Physik, Technische Universität Dortmund, D-44221 Dortmund, Germany; [e]Department of Physics and Astronomy, Dartmouth College, Hanover, NH 03755; and [f]Department of Physics, CUNY-City College of New York, New York, NY 10031

Contributed by Alexander Pines, August 24, 2018 (sent for review April 26, 2018; reviewed by Daniella Goldfarb, Songi Han, and Robert Tycko)

Dynamic nuclear polarization (DNP) has enabled enormous gains in magnetic resonance signals and led to vastly accelerated NMR/MRI imaging and spectroscopy. Unlike conventional *cw*-techniques, DNP methods that exploit the full electron spectrum are appealing since they allow direct participation of all electrons in the hyperpolarization process. Such methods typically entail sweeps of microwave radiation over the broad electron linewidth to excite DNP but are often inefficient because the sweeps, constrained by adiabaticity requirements, are slow. In this paper, we develop a technique to overcome the DNP bottlenecks set by the slow sweeps, using a swept microwave frequency comb that increases the effective number of polarization transfer events while respecting adiabaticity constraints. This allows a multiplicative gain in DNP enhancement, scaling with the number of comb frequencies and limited only by the hyperfine-mediated electron linewidth. We demonstrate the technique for the optical hyperpolarization of ^{13}C nuclei in powdered microdiamonds at low fields, increasing the DNP enhancement from 30 to 100 measured with respect to the thermal signal at 7T. For low concentrations of broad linewidth electron radicals [e.g., TEMPO ((2,2,6,6-tetramethylpiperidin-1-yl)oxyl)], these multiplicative gains could exceed an order of magnitude.

dynamic nuclear polarization | nuclear magnetic resonance | electron spin resonance | hyperpolarization | nitrogen-vacancy centers

Dynamic nuclear polarization (DNP)—the process of polarizing (cooling) nuclear spins to a spin temperature far lower than the lattice temperature (1, 2)—has emerged as a technological breakthrough that serves as the starting point for a wide range of applications, including signal enhanced spectroscopy (3) and imaging (4), and for state initialization in quantum information processing and metrology (5). Indeed, magnetic resonance (NMR and MRI) signals from hyperpolarized nuclear spins can be enhanced by several orders of magnitude, allowing enormous gains, even approaching a million-fold, in experimental averaging time. This has opened up avenues for the sensitive probing of phenomena, species, and surfaces (6), whose detection would otherwise have remained intractable.

In its simplest manifestation, DNP involves the use of electrons whose polarization is transferred to the nuclear spins via MW irradiation (2), allowing a polarization enhancement $\varepsilon \lesssim \gamma_e/\gamma_n$, where $\gamma_{e,n}$ are the gyromagnetic ratios of the electron and nuclear spins, respectively. Resonant polarization transfer between electron and nuclear spin is achieved via MW excitation. Depending on the concentrations of the electron and nuclear spins in the insulating solid, the transfer can be mediated by thermal mixing, the cross effect, the solid effect, and even the Overhauser effect. However, several common (e.g., nitroxide-based) electron-polarizing agents have large *g*-anisotropy and severely inhomogeneously broadened electronic linewidths that scale rapidly with field and can be as broad as 0.5 GHz at high fields (>3T) (7–10). This broadening limits the number of spins contributing to the resonant energy exchange at a particular MW frequency. Similar problems can exist even at low fields for some systems. For instance, Nitrogen Vacancy (NV) center defects in diamond (11, 12) have garnered much attention as optical hyperpolarizing agents because the NV electrons can be fully optically polarized at room temperature (13), opening the possibility for DNP enhancements larger than traditional bounds set by the gyromagnetic ratios, without the need for cyrogens. Interest has been particularly focused on "hyperpolarized nanodiamonds," because their inherently high surface area makes them attractive for the optical hyperpolarization of liquids brought in contact with them (14). While this has been a long-sought goal, technical challenges presented by the NV electrons make the production of hyperpolarized nanodiamonds challenging. In particular, the spin-1 NV centers have significant broadening on account of different crystallite orientations having different frequencies, giving rise to spectra broadened by >1 GHz even at modest (30 mT) fields. Unsurprisingly, precise energy matching to the nuclei in all these situations is challenging to achieve. Indeed, DNP traditionally has relied largely on *cw*-MW techniques (solid and cross effects), where a single frequency is saturated (15, 16), and consequently for static samples, only a small fraction of the broad electron spectrum directly contributes to the obtained enhancement.

In principle, however, significant gains in polarization enhancements can be achieved by exploiting the full broad electron

Significance

Dynamic nuclear polarization (DNP) can lead to rapidly accelerated NMR spectroscopy and MRI imaging via significant magnetic resonance signal gains. We develop a technique of microwave frequency comb DNP that is especially suited to broad-spectrum electron radicals widely used for DNP in a variety of contexts. The frequency comb allows one to overcome the bottleneck set by slow electron sweeps, increasing the effective number of polarization transfer events and resulting in a multiplicative gain in DNP signal enhancement. We demonstrate the technique by increasing the DNP enhancement from 30 to 100 measured with respect to the thermal signal at 7T in powdered diamond with optically polarizable defect centers and discuss its applications more widely for a variety of DNP radicals.

Author contributions: A.A. and A.P. designed research; A.A., R.N., K.L., X.L., B.S., G.W., and E.D. performed research; J.A.R., D.S., C.R., and C.A.M. advised on several aspects on experiments and theory; A.A. analyzed data; and A.A. wrote the paper.

The authors declare no conflict of interest.

Reviewers: D.G., Weizmann Institute of Science; S.H., University of California, Santa Barbara; and R.T., NIH.

[1]To whom correspondence may be addressed. Email: pines@berkeley.edu or ashokaj@berkeley.edu.

This article contains supporting information online at www.pnas.org/lookup/suppl/doi:10.1073/pnas.1807125115/-/DCSupplemental.

Published online October 2, 2018.

linewidth for DNP via more sophisticated quantum control on the electron spins, wherein every electron "packet" directly contributes to the DNP process (17). In this paper, we demonstrate a strategy to achieve this for the case of strongly anisotropic radicals in the limit of low (dilute) concentrations, where inter-electron couplings can be neglected—a situation pertinent for a wide class of nitroxide radicals and endogenously radicals native to several systems (18). Since savings in experimental time scale $\propto \varepsilon^2$, methods to increase hyperpolarization efficiency will directly translate to accelerated spectroscopy and imaging. Indeed, a surge in recent interest in DNP control techniques has been fueled by advances in instrumentation [sources (19, 20) and synthesizers (21)] that enable the rapid and coherent manipulation of electrons at high fields (22, 23). Particularly attractive among them is the use of frequency or field-swept techniques [e.g., integrated solid effect (ISE)] (24) that are suited to exploiting the wide electron bandwidth while only requiring modest MW power.

Principle

The DNP process underlying these techniques can be described as traversals of a level anticrossing (LAC) in an electron–nuclear dressed basis (Fig. 1). Polarization transfer occurs via Landau–Zener (LZ) tunneling (25), the onus of thermal contact being placed on maintaining adiabaticity during the sweep. The DNP transfer efficiency, governed by the tunneling probability, is given by $\varepsilon \propto \exp(-E_g^2/\dot{\omega})$, where $\dot{\omega}$ is the sweep rate and E_g is the effective energy gap, and depends on several parameters including the electron Rabi frequency Ω_e (24), hyperfine coupling to the target nucleus, and orientation. Despite harnessing the full electron linewidth, the frequency sweeps are often slow, and the requirement of adiabaticity sets bounds on the rate of polarization transfer. To illuminate this in more detail, let us assume an inhomogeneous electron linewidth $\mathcal{B}$, leading to a single traversal time $T = \mathcal{B}/\dot{\omega}$. Each electron frequency packet, however, has repolarized within a time $t_{\text{repol}} \leq T_{1e} \ll T$ and is available again for DNP transfer but instead has to wait the full period T when the subsequent sweep leads to the next polarization transfer event. Since the nuclear polarization is proportional to the total number of sweeps T_{1n}/T, the slow sweeps set a bottleneck on the DNP process, since an increasing bandwidth $\mathcal{B}$ leads to a longer period T. For instance, for the typical case of TEMPO at 3.35T and 50 K, $\mathcal{B} \approx 0.5$ GHz, and considering $\Omega_e = 1$ MHz (7), $T = 500$ ms, which far exceeds the inherent repolarization time, $T \gtrsim \mathcal{B}/\Omega_e^2 \gg T_{1e} \approx 1$ ms (7, 26).

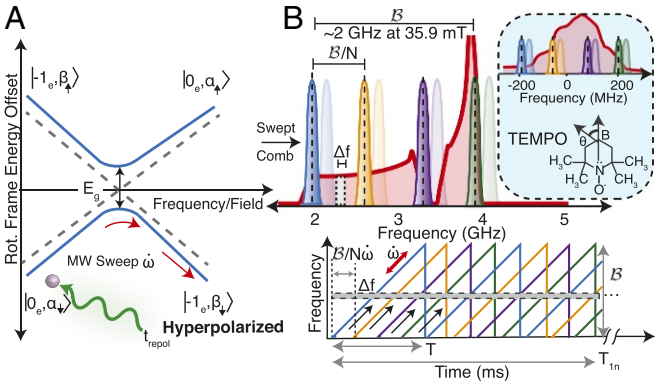

Fig. 1. Frequency comb enhanced DNP. (*A*) Hyperpolarization processes via frequency/field swept techniques are effectively Landau–Zener traversals of level anticrossings in a dressed electron–nuclear basis. The electron is repolarized every t_{repol}, and sweeps with an adiabatic scan rate $\dot{\omega}$ lead to polarization transfer. E_g refers to the energy gap. Levels shown here are for the NV center–^{13}C spin system. (*B*) Principle. Microwave (MW) frequency comb sweeping the entire inhomogeneously broadened electron spectrum (with linewidth $\mathcal{B}$) allows a repeated polarization transfer event with every successive comb frequency and produces a multiplicative boost in DNP enhancement. Red shaded area shows the spectrum for NV center electrons in diamond powder at 35.9 mT. The N comb frequencies can be as close as Δf, the hyperfine-mediated linewidth (shaded), and sweep every electron packet as often as t_{repol}. (*Inset*) A similar method could be applied to broadline electron radicals like TEMPO ((2,2,6,6-tetramethylpiperidin-1-yl)oxyl), shown here 3.35T with the spectrum centered at 95 GHz (7). (*Lower*) Time domain implementation through multiple cascaded frequency sweepers, illustrating the ability to maintain the adiabatic rate $\dot{\omega}$ while increasing the effective number of sweeps by N.

In this paper, we demonstrate a simple method to overcome this bottleneck, increasing the effective number of polarization transfer events while maintaining the optimal adiabatic sweep rates set by LZ conditions. Our method involves a swept MW frequency comb that coherently and simultaneously sweeps the entire electron linewidth $\mathcal{B}$ at $\dot{\omega}$, while maintaining adiabaticity for each sweep over an individual electron packet (see Fig. 1*B*). This allows repeated polarization transfer from each successive sweep of the comb, allowing one to gain a multiplicative DNP enhancement boost. Intuitively, the individual comb teeth can be as close as the electron linewidth Δf in frequency and can sweep each electron packet as often as t_{repol}, allowing an enhancement gain $\varepsilon \to N\varepsilon$. Since we work in the dilute electron limit, this electron packet linewidth predominantly arises due to hyperfine interactions with the surrounding nuclei. For the case of 10 mM TEMPO, for instance, this corresponds to a comb teeth separation of $1/T_M = 66$ kHz (29), where T_M is the phase memory time. Note that T_M serves here as a lower bound for the electronic T_{2e}, since phenomena such as spectral and instantaneous diffusion reduce T_M relative to T_{2e} (30). Without having to take into account specific details of the DNP mechanism in operation, one could bound the maximum enhancement gain $N \leq \min\{\mathcal{B}/\Delta f, \mathcal{B}/\dot{\omega}t_{\text{repol}} \approx \mathcal{B}/\Omega_e^2 T_{1e}\}$. The payoffs in hyperpolarization enhancements stemming from this multiplicative boost can be significant—for TEMPO, it could exceed an order of magnitude. More importantly, since the MW power for each sweep remains Ω_e, the technique can be relatively easily implemented with existing technology—the frequency comb being constructed by time-cascading sweeps from N separate low-power amplifiers (Fig. 1*B*).

While more generally employable, here we demonstrate its application to ^{13}C hyperpolarization in diamond particles via optically polarized electron spins associated with NV center defects. We have recently developed a method for optical ^{13}C DNP in powdered diamond at room temperature (27), using a combination of laser and swept MW irradiation at low magnetic fields ($B \sim 1$ to 30 mT). The DNP mechanism itself is a low-field complement to ISE, working in the regime where $\omega_L < |A|$, where $\omega_L = \gamma_n B$ is the nuclear Larmor frequency. The NV centers are inhomogenously broadened to a powder pattern with bandwidth $\mathcal{B} \approx 2\gamma_e B$, and here too the slow rate of MW sweeps over $\mathcal{B}$ limit the overall achievable nuclear polarization.

Low-Field ^{13}C DNP in Diamond Powder

Fig. 2*A* presents the hyperpolarization sequence. Laser irradiation polarizes the NV centers to the $m_s = 0$ state, a feature that occurs independent of field. We estimate the resulting NV electron polarization to be close to 100% in our experiments. Simultaneously applied swept MW irradiation (with Rabi frequency $\Omega_e \lesssim \omega_L$) causes the transfer of polarization to ^{13}C nuclei in the surrounding lattice. As described in Fig. 2*A*, the frequency-swept MW is applied in a sawtooth pattern for ~60 s. The DNP occurs independent of the orientation of the NV center axis in each crystallite, allowing the hyperpolarization of the entire high surface area powder (27). We evaluate the obtained hyperpolarization by benchmarking the polarization enhancement against the room temperature thermal equilibrium signal at 7T by

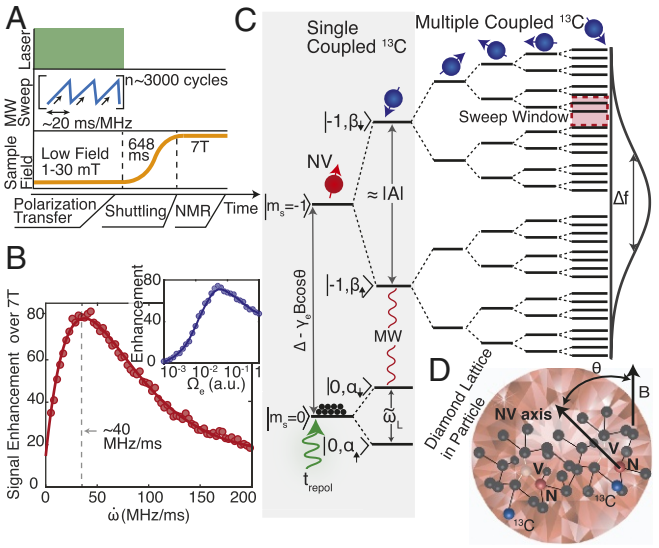

Fig. 2. ^{13}C hyperpolarization in diamond powder. (*A*) Sequence of events. Room temperature ^{13}C DNP from optically pumped NV centers is achieved via MW sweeps at low-field B = 1 to 30 mT under continuous 532 nm optical illumination. Bulk polarization is inductively detected by sample shuttling to 7T. (*B*) Sweep rate. DNP dependence on MW sweep rate shows an optimal $\dot{\omega}$ set by adiabaticity constraints. (*Inset*) Dependence on Rabi frequency Ω_e. (*C*) DNP mechanism. Energy levels of an NV electron and a single ^{13}C nuclear spin hyperfine coupled with A (gray box), in the low-field regime where nuclear Larmor frequency $\omega_L \lesssim |A|$. For simplicity, the $m_s = +1$ manifold is not shown. For an NV center coupled to multiple ^{13}C nuclei, one obtains a broadened ESR line by Δf. Sweeping over any window (shaded) leads to hyperpolarization and signal proportional to the local density of states. (*D*) Diamond lattice in a microparticle. NV axes are randomly oriented with respect to the field B, represented here by the angle θ.

sample shuttling (see Fig. 2*A*). We note that the sample shuttling time (≈648 ms) is longer than the electron T_{1e} but small compared with the nuclear ^{13}C lifetime, $T_{1n} > 120$ s at $B > 100$ mT. Fig. 2*B* details the typical dependence on MW sweep rate $\dot{\omega}$ and Rabi frequency Ω_e, both of which have optimal values set by adiabaticity constraints of the underlying microscopic DNP mechanism.

To intuitively understand the main features of the DNP mechanism, let us first consider the energy level structure of an NV center coupled to a single ^{13}C nuclear spin (Figs. 2*C* and 3). We work at low fields where $\omega_L < |A|$, and the dominant nuclear quantization axis in the $m_s = \pm 1$ manifolds is set by the hyperfine coupling, referred to as $\beta_{\uparrow,\downarrow}$ in Fig. 2*C*. The $m_s = 0$ state is magnetically silent, and in that manifold, the nuclear eigenstates $\alpha_\uparrow$ and $\alpha_\downarrow$ are dominated (for weakly coupled ^{13}C) by the Zeeman field with a second order correction from the hyperfine field, $\widetilde{\omega}_L \approx \omega_L + \frac{\gamma_e B A \sin\theta}{\Delta - \gamma_e B \cos\theta}$, where $\Delta = 2.87$ GHz is the zero-field splitting and θ is the angle from the applied field to the N-to-V axis (Fig. 2*D*). It is the relatively weakly coupled ^{13}C nuclei, $|A| \lesssim 1$ MHz, that participate most strongly in the hyperpolarization process (27) (*SI Appendix*).

Crucially, the large separation between the nuclear eigenstates in the $m_s = \pm 1$ manifolds and the low MW powers used ensures that the swept MWs sequentially excite a set of transitions that drive the polarization transfer. This manifests as a pair of LZ crossings in the rotating frame. Fig. 3 (reproduced from ref. 27) shows this in the $m_s = -1$ manifold considering positive and negative A_{zz} hyperfine couplings, where crossings occur between the states $|0,\alpha_\uparrow\rangle \leftrightarrow |-1,\beta_\uparrow\rangle$ and $|0,\alpha_\downarrow\rangle \leftrightarrow |-1,\beta_\downarrow\rangle$. Under the condition that one is adiabatic with respect to the larger energy gap and positive A_{zz} (see Fig. 3*A*), traversal through the level-anticrossings leads to a complete (bifurcated) transfer of population starting from the states $|0,\alpha_{\uparrow(\downarrow)}\rangle$, causing a bias in the system that hyperpolarizes the nuclei to the state $\alpha_\uparrow$. This simple model also captures why experimentally we find that the ^{13}C DNP sign depends only on the direction of the MW sweep, hyperpolarized aligned (antialigned) to B under MW sweeps from low to high (high to low) frequencies (27). While the laser is applied simultaneously with the MW sweep, it is of sufficiently low power that the optical repolarization of the NV takes place far away from the LZ events. The optimal sweep rates (see Fig. 2*B*) are set by adiabaticity constraints that maximize the differential LZ transfer probability between the two pairs of level-anticrossings and depend both on the Rabi frequency as well as on the hyperfine coupling and orientation (28) (*SI Appendix*). While considering the more realistic scenario of multiple ^{13}C nuclei coupled to the NV center, one obtains a continuum of levels stemming from the hierarchy of the hyperfine interactions, the closeby ^{13}Cs dominating the spectral widths. The density of states reflects the underlying hyerfine-broadened electron linewidth. Sweeping over any small spectral window in the broadened line (Fig. 2*C*) still leads to hyperpolarization, the sign of which depends on the direction of sweep (see Fig. 5*A*).

Even with this brief description, it is already apparent why the hyperpolarization is inefficient with a single sweeper. The electron resonance frequencies $\Delta \pm \gamma_e B \cos\theta$ are orientation-dependent, and in a randomly oriented powder, the ESR spectrum is broadened to $\mathcal{B} = 2\gamma_e B \approx 1.12$ GHz at 20 mT. This is shown in Fig. 5*A*, where we indirectly map the NV center ESR spectrum at 27.7 mT from the ^{13}C hyperpolarization enhancement by performing DNP over small (100 MHz) windows swept across in frequency space. The obtained spectrum is a convolution of the ESR spectrum with the used sweep window, and the two extremities of the spectrum correspond to the zero degree orientations. The experiment in Fig. 5*A* was performed on a collection of ≈300 diamond microparticles (Element6) of 200 μm size containing a natural abundance (1.1%) ^{13}C and ≈1 ppm of NV centers. Since both the $m_s = -1$ and $m_s = +1$ manifolds contain all of the NV center electron packets, it is sufficient to just sweep over one of them to obtain the optimal hyperpolarization on the ^{13}C nuclei. However, the sweep widths required in the $m_s = -1$ manifold, spanning the 0° (at frequency $f_0 = \Delta \mp \gamma_e B$) and 90° ($f_{90} = \frac{1}{2}[\Delta + \sqrt{\Delta^2 + (2\gamma_e B)^2}]$) NV center orientations, are still rather large (614 MHz at 20 mT). Due to fixed sweep rates $\dot{\omega}$ constrained by adiabaticity, the large $\mathcal{B}$ leads to a long MW sweep time $T = \mathcal{B}/\dot{\omega} \approx 16$ ms$> t_{\text{repol}}$ that far exceeds

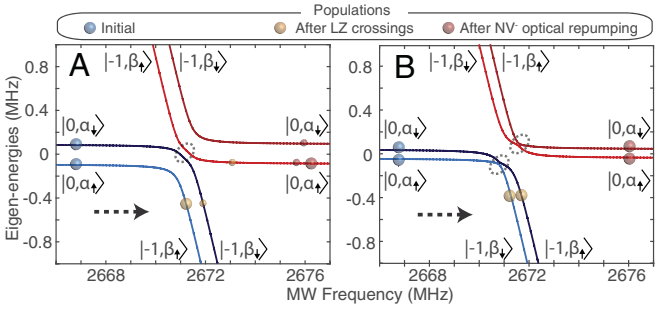

Fig. 3. Mechanism of polarization transfer. Calculated energy diagram in the rotating frame for an NV electron spin hyperfine coupled to a single ^{13}C nuclear spin (gray box in Fig. 2*C*) and corresponding to the $m_S = 0 \leftrightarrow m_S = -1$ subset of transitions (27, 28). *A* and *B* assume a hyperfine coupling $A_{zz} = +0.5$ MHz and -0.5 MHz, respectively, and B = 10 mT, θ = 45 deg., and $A_{zx} = 0.3|A_{zz}|$. Colored solid circles denote populations at different stages during a sweep in the direction of the arrow. Sweeping from low to high frequencies in the $m_s = -1$ manifold results in hyperpolarization buildup in a direction aligned with the magnetic field for positive A_{zz} (and analogous for $m_s = +1$ and negative A_{zz}).

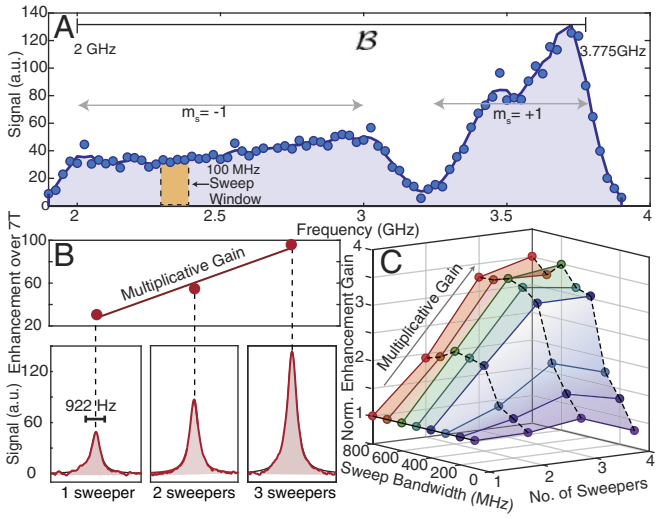

Fig. 4. Multiplicative DNP gains by frequency combs. (*A*) Indirect mapping of ESR lineshape. Exemplary NV center powder pattern at B = 27.7 mT indirectly obtained via ^{13}C DNP on a 100 MHz window swept across the ESR line. The ESR spectrum is orientationally broadened to $\mathcal{B} \sim$ 1.8 GHz. Sign of hyperpolarization is identical for the $m_s = \pm 1$ manifolds and depends only on the direction of the MW sweep. (*B*) Enhanced DNP gains. *Upper* shows the multiplicative boost in the DNP enhancements using a cascade of up to three MW sweepers, over a 700 MHz bandwidth at B = 13 mT. (*Lower*) Obtained hyperpolarized ^{13}C spectra at 7T after 30 averages. (*C*) Bandwidth dependence. Multiplicative gain factor using (up to) four cascaded sweepers, normalized by the use of a single one over the same band. Sweep bandwidths are centered at 2.8 GHz.

the repolarization time and bottlenecks the DNP enhancement. Given the laser power used ≈80 mW/mm^2, we estimate $t_{\mathrm{repol}} \sim$ 1 ms, on the same order as T_{1e} (31). The exact t_{repol} is challenging to measure especially on account of scattering, total internal reflections, and NV center charge dynamics.

Swept Frequency Combs for Multiplicative DNP Gain

Frequency combs provide an elegant means to overcome these bottlenecks, decoupling the rate at which the NV centers are swept over and the effective rates at which the LZ anticrossings are traversed for polarization transfer to the ^{13}C nuclei. Indeed, a swept MW frequency comb can maintain the adiabaticity constraints for a single sweep while increasing the cumulative number of sweeps in the total DNP period bounded by nuclear relaxation time T_{1n}. Moreover, in experiments where the NV repolarization rate $t_{\mathrm{repol}} \sim T_{1e}$, the swept frequency comb can ensure that the NV electrons are swept over sufficiently slowly so as to maximize the NV electron polarization at every sweep event.

MW frequency combs can be constructed by semiconductor lasers under negative optoelectronic feedback (32) and nonlinear mixing in tunneling junctions (33). In this paper, we follow a more brute-force approach instead, time-cascading MW sweeps generated by N voltage controlled oscillator (VCO) sources (*SI Appendix*). Fig. 5*B* shows the effect of using a frequency comb for DNP in the NV–^{13}C system. The DNP enhancement gains are significant, scaling linearly with N and allowing a multiplicative boost to the DNP enhancement over 7T from 30× to 100×. This constitutes an order of magnitude decrease in averaging time for the same signal-to-noise ratio (SNR). In the experiments, all of the sources sweep the entire bandwidth $\mathcal{B}$, and the frequency ramps are time-shifted by $\mathcal{B}/(N\dot{\omega})$ so as to maximize the period between successive sweeps (Fig. 1*B*). We refer the reader to *SI Appendix* for a discussion of several implemental aspects.

The cascaded sweeps entail an increase of the total MW power seen by the sample. For DNP mechanisms (e.g., ISE) where the energy gap (see Fig. 1) is predominantly determined by the electron Rabi frequency, using a higher MW power leads to a faster $\dot{\omega}$, and the same gains in principle can be achieved by the use of a single sweeper with higher power. However, even in this case, there are several technological advantages of using swept frequency combs for DNP. The costs of MW sources and amplifiers scale rapidly (≈ quadratically) with power (34), but using a cascade of N low-power amplifiers leads to only a linear cost scaling. Moreover, it is easier to directly synthesize slower frequency sweeps (19), for instance using inexpensive arbitary waveform generators and mixers (see *SI Appendix*), and using combs provides gains over field-swept modalities.

Limits of Multiplicative DNP Gains

Let us finally evaluate the factors affecting the ultimate limits to the multiplicative enhancement gain. In Fig. 5*C*, for a fixed $\dot{\omega}$, we vary the sweep bandwidth, equivalent to bringing the frequency comb sweeps closer in frequency and time. We measure the multiplicative gain by normalizing the signal of N sweepers against that from a single one. We observe that when the frequency comb teeth are separated by under ≈50 MHz ($\gg \Omega_e \approx$ 430 kHz), there is first a saturation in the DNP boosts and subsequent drop. We ascribe this to the inherent limit set by hyperfine mediated electron broadening Δf in the powder pattern (see also Fig. 4)—Δf here being the width of each individual NV center electron packet. When two sweeps occur simultaneously on different parts of the ESR line corresponding to a single NV center (Fig. 2*C*), there is interference between them and consequently lower efficiency in the hyperpolarization transfer.

Similar experiments allow us to quantify the optimal spacing between successive comb teeth. In Fig. 6, we change the phase ϕ between the time-cascaded ramps (e.g., in Fig. 1*B*) that generate the swept frequency combs. More intuitively, this phase directly corresponds to the frequency separation between the successive comb teeth as indicated in Fig. 6, *Lower*. Changing the phase has the effect of varying the frequency comb teeth separation over the fixed sweep bandwidth by $\phi\mathcal{B}/(2\pi)$ and the time period between successive electron sweeps by $\phi\mathcal{B}/(2\pi\dot{\omega})$.

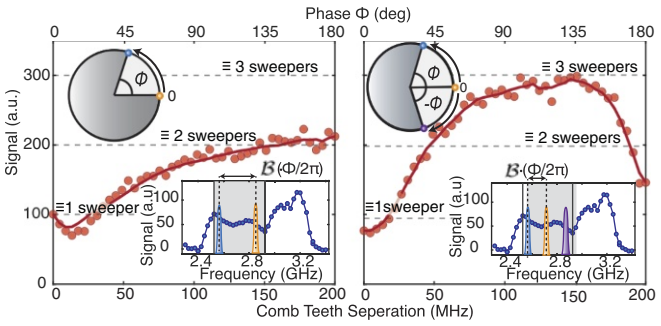

Fig. 5. Characterizing limits to multiplicative DNP gains by determining the optimal frequency separation for an N sweeper comb over a $\mathcal{B}$ = 400 MHz bandwidth ($m_s = -1$ manifold) and fixed optimal sweep rate $\dot{\omega}$= 39 MHz/ms. (*Inset*) Shaded region denotes sweep bandwidth over the experimentally obtained powder pattern at 12 mT. Sweepers are time cascaded with the ramps in Fig. 1*B* shifted by a phase ϕ (upper axis), translating to a frequency separation of the comb teeth by $f = (\phi/2\pi)\mathcal{B}$ (lower axis). We study ^{13}C DNP enhancements for (*Left*) two and (*Right*) three sweepers, with phases set to $\{0, \phi\}$ and $\{-\phi, 0, \phi\}$, respectively. *Insets* show them explicitly as phasors and in frequency domain. Data demonstrates that time ramps should be optimally phase shifted by $\phi_{\mathrm{opt}} = 2\pi/N$ for maximum DNP gains. As expected when $\phi = 0$, there is no gain in using N sweepers over a single one (lower dashed line), and for $\phi = 180°$, two and three sweepers provide similar enhancement (upper dashed line). Solid lines are guides to the eye.

Intuitively, one would expect that the t_{repol} and Δf limits would require that the comb teeth be maximally separated in both frequency and time, entailing a frequency separation of $\mathcal{B}/N$ and phase separation $\phi_{opt} = 2\pi/N$. Fig. 6 confirms this simple picture. Interestingly, it also demonstrates how the enhancement gains arise from the use of multiple sweepers. When all ramps have the same phase, the enhancement from the comb is identical to that using a single sweeper (dashed line in Fig. 6), increasing as the ramps are phase-shifted, with the expected optimal DNP gains at phase separation ϕ_{opt}. The plateaus in Fig. 6 indicate that the enhancement gains are achievable as long as the comb teeth are separated beyond Δf.

To make this more concrete, in Fig. 4, we perform DNP on single crystals with different ^{13}C enrichment. The crystals have ≈1 ppm NV centers, and since we are in the dilute electron limit, the electron packet linewidths are dominated by couplings to the ^{13}C nuclei. Moreover, the crystals are oriented parallel to the [100] direction such that all N–V axes are equivalent and at the magic angle to the polarizing field B and have the same frequency, hence eliminating inhomogeneous broadening. This is most evident in Fig. 4*A*, which demonstrates the electron spectrum mapped via ^{13}C DNP, evidenced by the mirror symmetry in the obtained DNP signals with opposite sweep directions. While we had considered the hyperpolarization mechanism in the context of weakly coupled ^{13}C nuclei, Fig. 4*A* also provides direct insight into strongly coupled first shell nuclei. The asymmetry in the obtained ESR spectra directly reports on the polarization of the first shell ^{13}C spins. Indeed, the difference signal obtained from alternate sweep directions (black line in Fig. 4*A*) shows the characteristic ESR spectrum with satellites from first-shell ^{13}C nuclei strongly hyperfine-coupled by ∼130 MHz (35).

The fact that hyperfine couplings dominate the ESR linewidths (Fig. 2*C*) are most evident in Fig. 4*B*, where we measure Δf with increasing ^{13}C enrichment. In Fig. 4*C*, we study the DNP enhancements with one and two cascaded sweepers for varying sweep bandwidths and fixed $\dot{\omega}$ over these hyperfine broadened lines, choosing as a representative example the 10% enriched sample studied in Fig. 4*A*. The sweep bandwidths in these experiments are centered at the peak of the ESR spectrum. Let us first consider the case of a single sweeper (blue line in Fig. 4*C*). The enhancement increases with sweep bandwidth, reaching an optimal value when $\mathcal{B} \approx \Delta f$, corresponding to the MWs being applied most efficiently over the electron spectrum. While using two sweepers, on the other hand, there are no DNP enhancement gains when the comb frequencies are closer than Δf. Note that in these experiments we space the comb teeth (optimally) by half the bandwidth. The maximum enhancement occurs when the comb separation is Δf, corresponding to a total sweep bandwidth of $2\Delta f$, a strong indication that the two sweepers interfere with each other when simultaneously used on the hyperfine broadened electron line. Performing similar experiments on the samples with different ^{13}C enrichment allows us to quantify the sweep bandwidths at which two sweepers perform better than a single one (see *SI Appendix*). The optimal sweep bandwidths for one and two sweepers are elucidated in Fig. 4 *C*, *Inset*, and they closely match the intrinsic Δf linewidths in Fig. 4*B*, scaling with ^{13}C enrichment. Overall, therefore, in the ultimate limit, the frequency combs approach an excitation of all Δf-wide electron packets at once, sweeping them as often as t_{repol}—approaching the efficiency of a pulsed DNP experiment over the entire electron bandwidth.

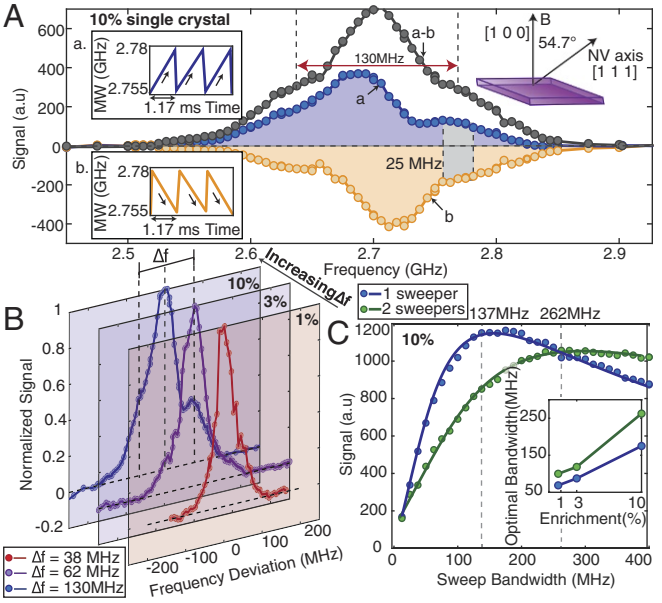

Fig. 6. ESR linewidth limits to enhancement gain elucidated by performing ^{13}C DNP with all NV axes at magic angle θ_M = 54.7° to B (*Inset*). (*A*) ESR lineshape of a 10% enriched ^{13}C crystal mapped indirectly via DNP on a 25 MHz window at B = 10.5 mT. Blue (yellow) points show obtained DNP enhancements sweeping MWs from low to high (high to low) frequency with $\dot{\omega} = 21$ MHz/ms (*Insets* show schematic ramps for an exemplary window). Hyperpolarization sign depends on the direction of the MW sweep, and the mirror symmetry of the lineshapes reflects the local density of states (Fig. 2*C*). Black line is the difference signal and faithfully represents the hyperfine broadened NV center ESR spectrum with Δf dominated by coupling to first shell ^{13}C nuclei, hyperfine coupled by ∼130 MHz. (*B*) Effects of ^{13}C enrichment. Indirectly mapped ESR spectra of 1%, 3%, and 10% ^{13}C-enriched single crystals under DNP with low to high frequency sweeps, showing increasing Δf [legend: full width at half maximum (FWHM)] with enrichment. (*C*) Cascaded sweeps over a hyperfine broadened line. For the 10% ^{13}C single crystal in *A*, we perform DNP with one and two cascaded sweepers over a varying bandwidth centered at 2.688 GHz (peak of a in *A*). Results indicate that frequency comb teeth have to be separated beyond Δf to provide enhancement gains. (*Inset*) Optimal sweep bandwidths while using one and two cascaded sweepers for crystals of different ^{13}C enrichment.

Applications to Conventional DNP

The most direct applications of the current method are for DNP in systems with endogenous radicals [e.g., Si, diamond surfaces (36)] or where they can be optically excited (37), since the linewidths of such radicals are hard to control. For radicals with a large g-anisotropy (e.g., TEMPO, Galvinoxyl) and low concentrations, the large inhomogeneous broadening leads to an inefficient transfer and lower DNP enhancement due to the (differential) solid effect. Indeed, experiments are typically performed at higher radical concentrations [>20 mM (29)], where DNP can occur via the cross effect (16), with significantly faster growth times. However, the higher radical concentrations lead to a broadening of the observed NMR lines (38) and are a challenge for high-resolution spectroscopy applications (39). The use of swept frequency combs can dramatically improve DNP enhancement at low radical concentrations by enacting a transition to the ISE. Since ISE is bottlenecked by similar factors, the demonstrated gains in Fig. 5 should be directly transferable to ISE. The use of frequency modulation to implement ISE was recently demonstrated at X-band (23), and we anticipate large gains with frequency combs. While the increased reliance on spin diffusion will increase the growth time of the DNP signal, frequency combs offer the possibility of obtaining high DNP enhancements without concomitant NMR line broadening.

Conclusions and Outlook

We have experimentally demonstrated a simple and scalable technique to obtain multiplicative enhancement gains in DNP. The method entails a swept frequency comb to excite

the entire inhomogenously broadened electron bandwidth for polarization transfer. It can be implemented by cascading N sweeps from individual low-power sources/amplifiers to obtain a DNP enhancement boost $\propto N$, with ultimate limits set by the hyperfine-mediated electron linewidth and lifetime T_{1e}. As such, the technique affirms the notion that the electron spin control can significantly enhance DNP by harnessing the full power of the electron spectrum. We demonstrated its utility for the hyperpolarization of ^{13}C nuclei in diamond microparticles via optically pumped NV centers at room temperature, obtaining a 300% boost in DNP efficiency. When used for conventional polarizing radicals at high fields, the technique promises to yield DNP enhancement boosts in excess of one order of magnitude, with a relatively simple implementation using existing technology and only modest cost overheads.

ACKNOWLEDGMENTS. We acknowledge discussions with J. P. King, P. R. Zangara, and S. Dhomkar. C.A.M. acknowledges support from NSF Grants NSF-1401632 and NSF-1547830 and from Research Corporation for Science Advancement (Frontiers in Research Excellence and Discovery Award). C.R. acknowledges support from NSF Grant CHE-1410504.

1. Carver TR, Slichter CP (1953) Polarization of nuclear spins in metals. *Phys Rev* 92: 212–213.
2. Abragam A, Goldman M (1978) Principles of dynamic nuclear polarization. *Rep Prog Phys* 41:395–467.
3. Maly T, et al. (2008) Dynamic nuclear polarization at high magnetic fields. *J Chem Phys* 128:052211.
4. McCarney ER, Armstrong BD, Lingwood MD, Han S (2007) Hyperpolarized water as an authentic magnetic resonance imaging contrast agent. *Proc Natl Acad Sci USA* 104:1754–1759.
5. Foletti S, Bluhm H, Mahalu D, Umansky V, Yacoby A (2009) Universal quantum control of two-electron spin quantum bits using dynamic nuclear polarization. *Nat Phys* 5:903–908.
6. Lesage A, et al. (2010) Surface enhanced NMR spectroscopy by dynamic nuclear polarization. *J Am Chem Soc* 132:15459–15461.
7. Feintuch A, et al. (2011) A dynamic nuclear polarization spectrometer at 95 GHz/ 144 MHz with EPR and NMR excitation and detection capabilities. *J Magn Reson* 209:136–141.
8. Song P, Zhao Z, Xu X, Deng P, Xu J (2006) Growth and spectral properties of yb:fap single crystal. *Opt Mater* 29:471–474.
9. Hu KN, Bajaj VS, Rosay M, Griffin RG (2007) High-frequency dynamic nuclear polarization using mixtures of tempo and trityl radicals. *J Chem Phys* 126:044512.
10. Armstrong BD, Han S (2007) A new model for overhauser enhanced nuclear magnetic resonance using nitroxide radicals. *J Chem Phys* 127:104508.
11. Wrachtrup J, Jelezko F (2006) Processing quantum information in diamond. *J Phys Condens Matter* 18:S807–S824.
12. Ajoy A, Bissbort U, Lukin MD, Walsworth RL, Cappellaro P (2015) Atomic-scale nuclear spin imaging using quantum-assisted sensors in diamond. *Phys Rev X* 5:011001.
13. Fischer R, et al. (2013) Bulk nuclear polarization enhanced at room temperature by optical pumping. *Phys Rev Lett* 111:057601.
14. Chen Q, Schwarz I, Jelezko F, Retzker A, Plenio M (2015) Optical hyperpolarization of c 13 nuclear spins in nanodiamond ensembles. *Phys Rev B* 92:184420.
15. Hovav Y, Feintuch A, Vega S (2010) Theoretical aspects of dynamic nuclear polarization in the solid state—The solid effect. *J Magn Reson* 207:176–189.
16. Hwang CF, Hill DA (1967) Phenomenological model for the new effect in dynamic polarization. *Phys Rev Lett* 19:1011–1014.
17. Hovav Y, Feintuch A, Vega S, Goldfarb D (2014) Dynamic nuclear polarization using frequency modulation at 3.34 T. *J Magn Reson* 238:94–105.
18. Rej E, Gaebel T, Waddington DE, Reilly DJ (2017) Hyperpolarized nanodiamond surfaces. *J Am Chem Soc* 139:193–199.
19. Guy ML, Zhu L, Ramanathan C (2015) Design and characterization of a w-band system for modulated DNP experiments. *J Magn Reson* 261:11–18.
20. Yoon D, et al. (2016) Dynamic nuclear polarization by frequency modulation of a tunable gyrotron of 260 GHz. *J Magn Reson* 262:62–67.
21. Kaminker I, Barnes R, Han S (2017) Arbitrary waveform modulated pulse EPR at 200 GHz. *J Magn Reson* 279:81–90.
22. Hoff DE, et al. (2015) Frequency swept microwaves for hyperfine decoupling and time domain dynamic nuclear polarization. *Solid State Nucl Magn Reson* 72:79–89.
23. Can TV, Weber RT, Walish JJ, Swager TM, Griffin RG (2017) Frequency-swept integrated solid effect. *Angew Chem Int Edition* 56:6744–6748.
24. Henstra A, Dirksen P, Wenckebach WT (1988) Enhanced dynamic nuclear polarization by the integrated solid effect. *Phys Lett A* 134:134–136.
25. Zener C (1932) Non-adiabatic crossing of energy levels. *Proc R Soc Lond A* 137:696–702.
26. Shimon D, Hovav Y, Feintuch A, Goldfarb D, Vega S (2012) Dynamic nuclear polarization in the solid state: A transition between the cross effect and the solid effect. *Phys Chem Chem Phys* 14:5729–5743.
27. Ajoy A, et al. (2018) Orientation-independent room temperature optical 13 C hyperpolarization in powdered diamond. *Sci Adv* 4:eaar5492.
28. Zangara P, et al., Dynamics of frequency-swept nuclear spin optical pumping in powdered diamond at low magnetic fields. *Proc Natl Acad Sci USA*, in press.
29. Siaw TA, et al. (2014) Effect of electron spin dynamics on solid-state dynamic nuclear polarization performance. *Phys Chem Chem Phys* 16:18694–18706.
30. Schweiger A, Jeschke G (2001) *Principles of Pulse Electron Paramagnetic Resonance* (Oxford Univ Press, Oxford), on Demand.
31. Jarmola A, Acosta V, Jensen K, Chemerisov S, Budker D (2012) Temperature- and magnetic-field-dependent longitudinal spin relaxation in nitrogen-vacancy ensembles in diamond. *Phys Rev Lett* 108:197601.
32. Juan YS, Lin FY (2009) Microwave-frequency-comb generation utilizing a semiconductor laser subject to optical pulse injection from an optoelectronic feedback laser. *Opt Lett* 34:1636–1638.
33. Hagmann MJ, Efimov A, Taylor AJ, Yarotski DA (2011) Microwave frequency-comb generation in a tunneling junction by intermode mixing of ultrafast laser pulses. *Appl Phys Lett* 99:011112.
34. Joye CD, et al. (2006) Operational characteristics of a 14-W 140-GHz gyrotron for dynamic nuclear polarization. *IEEE Trans Plasma Sci* 34:518–523.
35. Rao KRK, Suter D (2016) Characterization of hyperfine interaction between an NV electron spin and a first-shell c 13 nuclear spin in diamond. *Phys Rev B* 94:060101.
36. Cassidy M, Ramanathan C, Cory D, Ager J, Marcus CM (2013) Radical-free dynamic nuclear polarization using electronic defects in silicon. *Phys Rev B* 87:161306.
37. Capozzi A, Cheng T, Boero G, Roussel C, Comment A (2017) Thermal annihilation of photo-induced radicals following dynamic nuclear polarization to produce transportable frozen hyperpolarized 13c-substrates. *Nat Commun* 8:15757.
38. Lange S, et al. (2012) The effect of biradical concentration on the performance of DNP-MAS-NMR. *J Magn Reson* 216:209–212.
39. Saliba EP, et al. (2017) Electron decoupling with dynamic nuclear polarization in rotating solids. *J Am Chem Soc* 139:6310–6313.